Int. J. Electrochem. Sci., 13 **(2018)** 10612 – 10625, doi: 10.20964/2018.11.36

International Journal of
ELECTROCHEMICAL
SCIENCE
www.electrochemsci.org

Electrospun Antimony Tin Oxide Nanofibers with Superior Stability as Anode Material for Li-ion Batteries

Ning Zhao[1,2,3], *Libo Deng*[2] ,*Dawei Luo*[3],*Shuting He*[1] *and Peixin Zhang*[1,2,*]

[1] School of Materials & Mineral Resources, Xi'an University of Architecture and Technology, Xi'an, Shanxi 710055, P.R China
[2] College of Chemistry and Environmental Engineering, Shenzhen University, Shenzhen 518060, China
[3] School of chemistry and biological application, Shenzhen Polytechnic,Shenzhen 518000,China
[*]E-mail: pxzhang@szu.edu.cn

Received: 23 July 2018 / *Accepted:* 8 September 2018 / *Published:* 1 October 2018

Tin oxide (SnO_2) is a promising alternative material to replace graphite as an anode material for lithium ion battery (LIB). However, bulky neat SnO_2 still suffers from serious pulverization and rapid decay of capacity during charging and discharging. In this study, to enhance the cyclic stability and rate performance of SnO_2–based anode, antimony tin oxide (ATO)-containing nanofibers were synthesized by a two-step process in this work, including electrospinning of $SnCl_2$/$SbCl_3$/PVP and calcination at 400°C-600°C in air. The electrospun fibers developed from solid to hollow structures through a Kirkendall diffusion process. All ATO nanofibers treated at different temperatures showed an extraordinary initial capacities, in the range of 1563 $mAhg^{-1}$-1711$mAhg^{-1}$ during the first discharge. Moreover, the fibers calcinated at 400 °C exhibited excellent cyclic stability, namely the capacity at the 200th cycle was 730 $mAhg^{-1}$ at a current density of 0.2Ag^{-1}, which was 76% of its capacity at the 2nd cycle. In addition, this material also displayed excellent rate performance, delivering 327 $mAhg^{-1}$ at 3.2Ag^{-1} after 60 cycles. These values were superior to those calcinated at 600°C, Because of its reduced volume, the carbon matrix provides a large surface area and a short diffusion length in the treated ATO fibers. provided by the carbon matrix in the 400°C-treated ATO fibers. These results revealed the importance of combining the buffering carbon phase with the nano-fibrous structure for the improvement of SnO_2-based electrode, and would pave the way for further enhancing the performance of anodes for LIBs.

Keywords: Antimony tin oxide; Hollow nanofibers; Anode; Li-ion battery

1. INTRODUCTION

Graphite has been used as an anode in major lithium-ion batteries (LIBs) for the past few decades . but it could not meet the future demands on even higher performance. Hence tremendous

efforts have been devoted to developing alternative current anode materials with higher storage capacity and longer life to replace the current anode material [1, 2].

Among the numerous novel candidates for such purpose, tin-based materials (Sn and/or SnO_2 and their composites) have attracted particular attention due to their high theoretical capacity (790 $mAhg^{-1}$ for SnO_2 and 990 $mAhg^{-1}$ for Sn), safe working potential and low toxicity [3, 4].

However, Sn and SnO_2 both suffer from severe volume change and pulverization which leads to rapid capacity loss, an issue exists also for other electrode material based on a single metal (or metal oxide). Two general methods have been proposed to alleviate the volume change and enhance the cyclic stability of tin-based material in literatures, namely the downsizing of crystalline particles and incorporation of active materials into a buffer matrix [5-7]. Anode based on various nanostructures of Sn such as SnSb alloy particles, graphene/SnO_2 nanocomposites, Sn/SnO_2@C nanofibers and ternary alloy of Sn-Ni-Cu-alloy@carbon nanorods have been reported [5, 8-10]. However, a capacity below 700 $mAhg^{-1}$ after 100 cycles is typically obtained and further improvement of the cyclic stability is desired for practical applications.[11]

Recent studies have shown that the combination of Sn nanoparticles with the nanostructure of one-dimensional buffer substrates, such as carbon fiber, is of great benefit to the mechanical stability of the morphology, and provides rapid transport of electrons and lithium ion pathways and large active sites for lithium storage [6]. Our previous studies also showed that the electrochemical performance of conventional (i.e. nanoparticles) electrode materials can be enhanced remarkably by creating nano-fibrous structure [10-14]. Furthermore, it has also been demonstrated that excellent cyclic stability can be achieved by alloying Sn with another metal which can independently store high amounts of lithium, due to that only one elements reacts with lithium at a time and the other acts as a buffer during that time period. However, nanofibers comprised of these binary metal oxides fabricated through a facile electrospinning method has not been reported yet.

In this study, ATO-containing nanofibers were synthesized by first electrospinning of a blended solution of $SnCl_2$, $SbCl_3$ and polyvinylpyrrolidone (PVP), which were then annealed in air. The electrospun nanofibers developed from solid to hollow structures when the temperature was increased from 400°C to 600°C due to Kirkendall diffusion effect. The performance of the ATO nanostructures as an anode for LIBs was investigated. The results show that, in calcining, the remaining carbon provides a large surface area and can buffer the change of volume during the charge-discharge process, so the cyclic stability and rate performance of the fiber are in the best condition.

2. EXPERIMENTAL

2.1 Synthesis of ATO-based anode materials

The ATO-containing nanofibers were prepared by electrospinning of precursor solution followed by a calcination process (Figure 1). PVP was dissolved in dimethamide (DMF) at room temperature to prepare the polymer solution with a concentration of 13%. The molar ratio of SnCl2·2H2O (analysis level) and SbCl3 (analysis level) salt was 1:1, which was mixed and dissolved in ethanol for 8 hours to prepare the solution with a total salt concentration of 12.%. A stable electrostatic spinning solution was obtained by mixing salt solution with PVP solution at a weight ratio

of 1:1 and stirring for 12 hours. The prepared solution was loaded into a plastic syringe, and the electrostatic spinning was performed with the flow rate of 1ml h-1, the distance from the needle to the collector was 12cm, and the voltage was 13v. Electrostatic spinning of nanofibers deposited on the oxidation of aluminum foil, and in 80 ° c in the oven drying 3 hours. Then, in the calcination and 600 ° c temperature range between the fibers in the air is heated. At 400° C ,500 ° C and 600 ° C to handle samples respectively called ATO - 400 , ATO-500,and ATO-600.

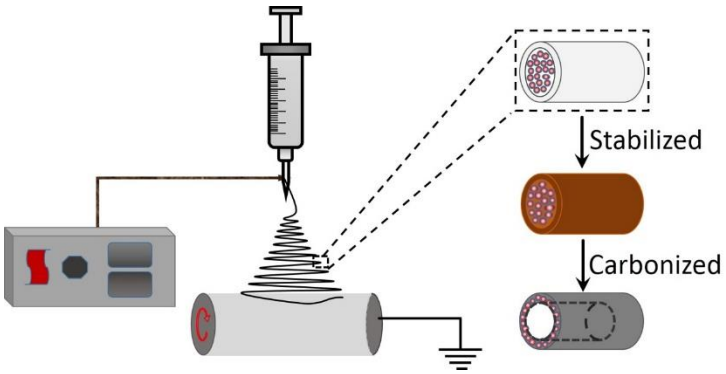

Figure 1. The preparation procedure of ATO-containing nanofibers.

2.2 Physical characterizations

The microcrystalline structure of the fiber was determined by Brook optics D8 advanced X-ray diffraction (XRD, λ= 1.54, CuKa radiation). Scanning electron microscopy (SEM) (Hitachi, S-3400N) and high resolution transmission electron microscopy (HRTEM) (Tecnai G2 F30) were used to study the morphology and structure of the composite. The chemical valence of surface components was analyzed by X ray photoelectron spectroscopy (XPS) system (ESCALAB 250Xi). The data are calibrated, and the fixed value of C1s peak is 284.7 eV. Thermogravimetric analysis (TGA, STA409PC) (TGA, STA409PC) measurement was performed from room temperature to 1000°C under a controlled heating rate of 10°C min^{-1} in air.

2.3 Electrochemical characterizations

A kind of slurry was prepared, which was composed of 85wt% active material, 5wt% acetylene black and 10wt%carboxymethyl cellulose (CMC) and styrene butadiene rubber (SBR). The electrodes were prepared by pressing them on copper foil and drying them at 120°C under vacuum for 10 hours. The active material is loaded on the copper foil with 1.2mg/cm^{-2}.

Then, metal lithium foil was used as a counter electrode assembly, 1M $LiPF_6$ dimethyl carbonate (DMC) (1:1 v/v) was used as an electrolyte, celegard 2400 was used as a separating agent, and a nanoparticle/copper foil was synthesized as an anode. Cycle performance and rate capabilities were evaluated using a CT2001A battery tester from 0.01 to 2.0 V (vs Li/Li^+). Cyclic voltammetry (CV) from 0.01 to 2.0 V (vs. Li/Li^+.) at 0.1mV/s and electrochemical impedance spectroscopy (EIS) in

the frequency range 10^{-2} to 10^{5} Hz and with an amplitude of 5 mV using electrochemical Workstation (CHI660A).

3. RESULTS AND DISCUSSION

The crystallite structure of nanofibers derived from pyrolysis of $SnCl_2/SbCl_3$/PVP composite was first characterized using XRD and the results are shown in Figure 2a. Reflections at 26.6°, 33.9°, 38.0°, 51.8°, 54.8°, 61.9°, 64.8° and 66.0° were observed for all calcinated nanofibers, which correspond to (110), (101), (200), (211), (220), (310), (112) and (301) planes of tetragonal tin antimony oxide (JCPDS no. 88-2348) and indicates the successful conversion of $SnCl_2$ and $SbCl_3$ into binary oxides of ATO with high crystallinity upon the heat treatment. In addition, the diffraction peaks become narrower as the temperature increases, suggesting the increase of the ATO crystallite size. For both anode and cathode of Li-ion batteries, carbon influences the electrochemical performances significantly and thus the carbon contents in the ATO samples were first determined using TGA.

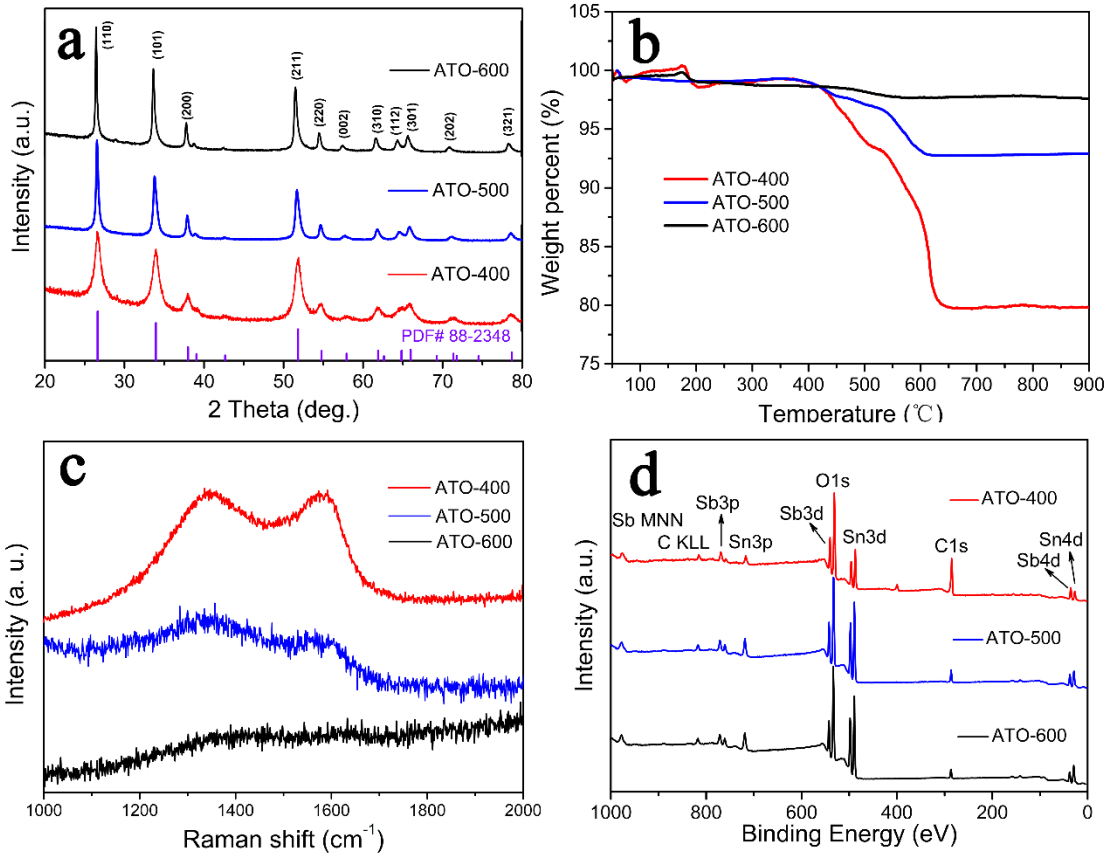

Figure 2. Structural characterizations: (a) XRD patterns, (b) TGA curves, (c) Raman spectra and (d) XPS spectra of ATO-400, ATO-500 and ATO-600 nanofibers.

The measurements (Figure 2b) suggest that there is still 18% of carbon remaining in ATO-400, which is due to incomplete degradation of PVP at this temperature (Figure S1 in the supporting information shows the TGA curve for PVP). The weight loss at 700°C, i.e. the content of carbon is 7%

for ATO-500 and only 2% for ATO-600. The existence of carbon residue was further confirmed by Raman spectroscopy (Figure 2c). Strong D and G bands characteristic to sp^2 hybridized carbon were seen from ATO-400, which became remarkably weaker in ATO-500 and were inappreciable in ATO-600, which further suggests the lower content of carbon in the latter two samples. Nevertheless, no diffraction from carbon crystallites was observed from the three samples. It is thus concluded that ATO nanofibers are composites consisting of amorphous carbon and ATO, although the carbon content in ATO-600 is negligible.

The surface composition and chemical state of the nanofibers were examined by XPS. The full spectrum is shown in Figure 2d. The range of binding energy peaks is 284.7 eV and 288.4 eV corresponds to carbon, the peak is located at 487.1 and 495.4 eV from Sn 3d5/2 and Sn 3d3/2, two peaks at binding energies of 530.8 and 540.4 eV are attributed to Sb 3d5/2 and Sb 3d3/2, and the peak at 531 eV can be assigned to O element (deconvolved peaks are shown in Figure S2) [12-14]. The intensity of carbon peak decreases progressively with the increase of calcination temperature, and it is still noticeable in ATO-500 and ATO-600. Understandably, XPS technology can only detect a few nanometer depths of a carbon-rich surface.

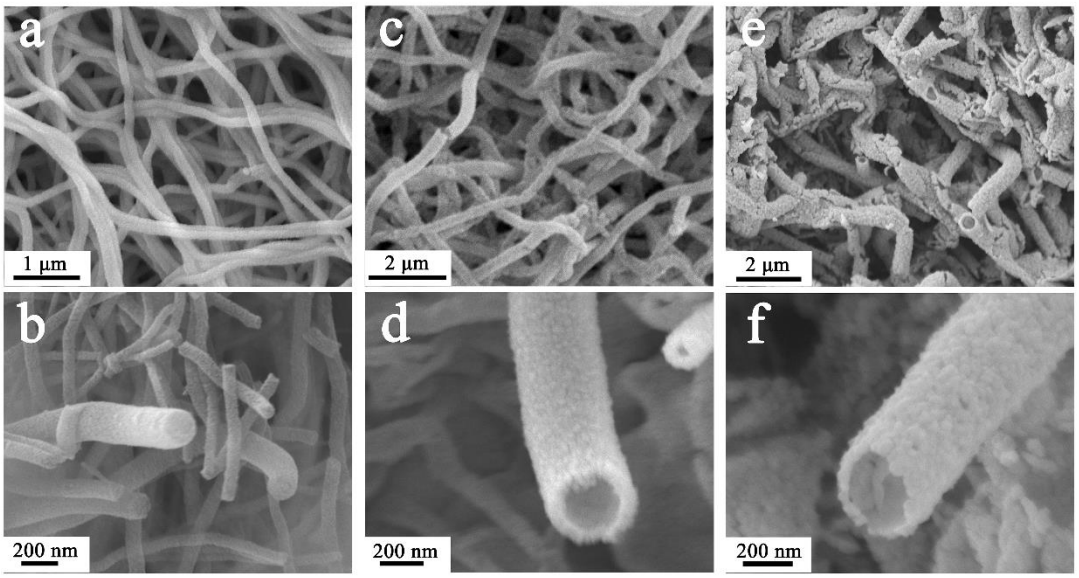

Figure 3. SEM images at different magnifications : (a) and (b) ATO-400, (c) and (d) ATO-500, and (e) and (f) ATO-600.

The morphology of the nanofibers was investigated using SEM. It can be seen from Figure 3 that the fibers develop from solid to hollow structures with the surface becomes more rough when the temperature increases from 400°C to 500°C. As the temperatures further increases to 600°C, the tubular structure retains but the wall becomes thinner and fragmentation is more frequently observed. Meanwhile, the diameter increased from 160 nm for ATO-400 to 200 nm for ATO-500 and further to 250 nm ATO-600. This increase might be due to that as the carbon component vanishes at a higher temperature, the contact between the ATO particles become more loose which gives rise to a larger diameter. ln addition, the SEM element map image (Figure S3) shows the uniform distribution of Sn,

Sb and O elements in the three samples. It was also noted that the molar ratio of Sn and Sb in all the calcinated nanofibers are similar to 1:1, which is close to the ratio between these two elements in the starting material.

The microstructure of the nanofibers was further investigated using HRTEM. The evolution from solid to hollow structures from 400°C to 600°C, as shown in Figures 4a-4c, agrees well with the SEM observation. It can be seen that isolated ATO nanoparticles are embedded in an amorphous carbon matrix in ATO-400, whereas ATO-500 and ATO-600 contain significantly less carbon and the rigid ATO becomes the continuous phase. Closer inspection clearly reveal lattice fringes with a separation of 0.34 nm and 0.26 nm in ATO-500 (Figures 4d and 4e), which correspond to the (110) and (101) plane of ATO crystallites, respectively. The selected area electron diffraction (SAED) pattern confirms the formation of highly crystalline ATO (Figure 4f).

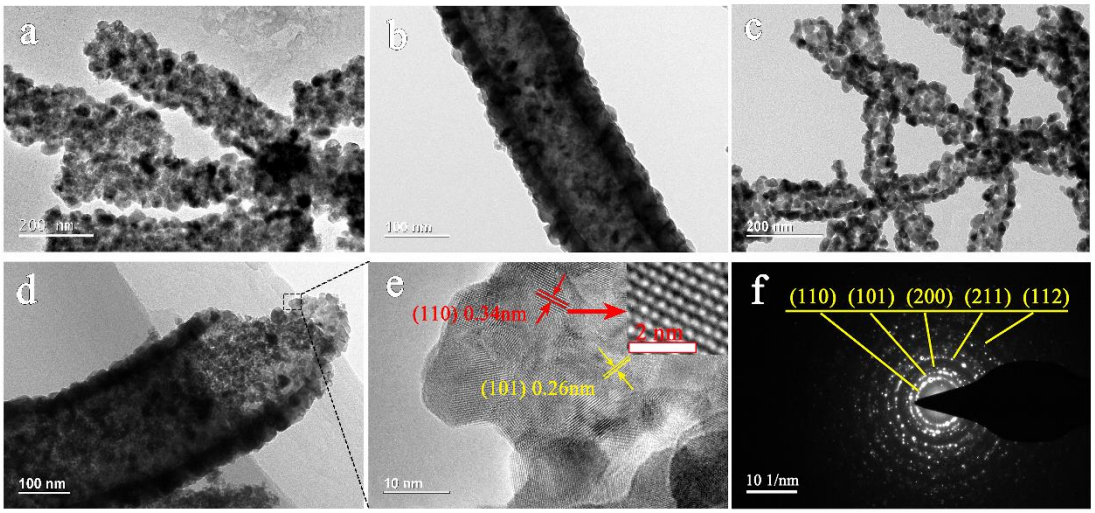

Figure 4. TEM images of the ATO nanofibers: (a) ATO-400, (b) ATO-500 and (c) ATO-600; (d) another ATO-500 fiber, (e) enlarged image and (f) SAED pattern for the highlighted area in (d).

A possible mechanism for the development of the morphology and structure for the nanofibers is proposed (Figure 5). During the heat treatment, since the temperature reaches 280 °C, $SnCl_2$ and $SbCl_3$ start to decompose near the surface of the fiber, and are easily oxidized to form SnO_2 and Sb_2O_3 particles, while the inner salt is deficient in oxygen. Thus, bidirectional concentration gradients, ie salt gradients and metal oxide gradients, form nanofibers in cross-section, leading to the "Kirkendall effect" and driving the diffusion of $SnCl_2$ and $SbCl_3$ from the core to the surface and SnO_2, Sb_2O_3 particles from the surface to the nanofibers Core. [1, 15-18]. The $SnCl_2$ (T_m~37.7°C) and $SbCl_3$ (T_m~73.4°C) melt diffuse much faster than the SnO_2 (T_m~1630°C) and Sb_2O_3 (T_m~656°C) particles. During this process, the metal salts were completely oxidized, and the PVP decomposed at the same time [15, 16]. Similarly, when the PVP decomposed to form CO_2, due to the lack of oxygen in the core of the nanofibers, bidirectional concentration gradients formed for PVP and O_2. Therefore, the PVP diffused from the core to the surface and O_2 from the surface to the core of the nanofibers, which gives

rise to a porous structure for the nanofibers and is particularly pronounced for ATO-400. The continuous consumption of carbon in the core region eventually led to a hollow structure and as the carbon vanishes as well as the ATO crystallites grows, the fibers become more fragile.

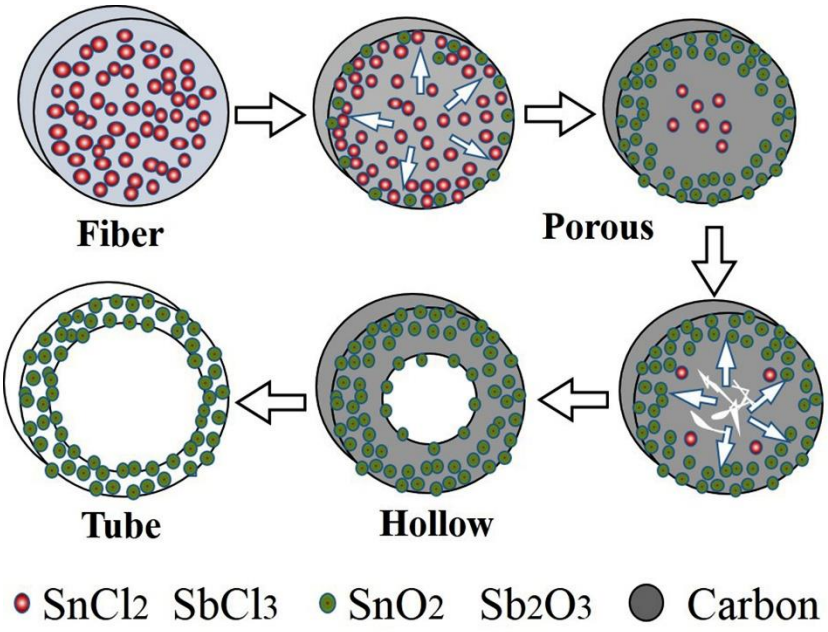

Figure 5. Proposed mechanism for the development of the structure of ATO nanofibers.

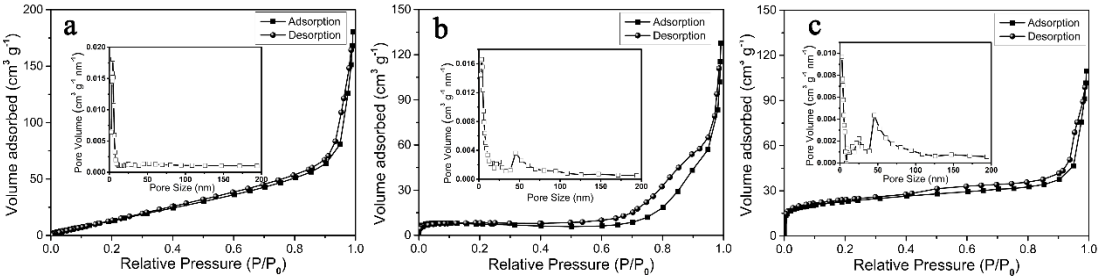

Figure 6. N_2 adsorption-desorption isotherms and pore size distribution of the ATO nanofibers.

Changes in surface area and pore size as measured by nitrogen adsorption/desorption methods also reflect the evolution of amorphous and microstructure. Figure 6 shows the nitrogen adsorption and desorption isotherms of ATO nanofibers and the corresponding Barrett-Joyna-Halenda (BJH) pore size distribution. The Brunauer-Emmet-Teller (BET) surface area decreased from 81.6 m^2 g^{-1} for ATO-400 to 34.2 m^2 g^{-1} for ATO-500 and 23.2 m^2 g^{-1} for ATO-600, whereas the average pore size increased from 2.52 nm to 4.42 nm and 10.89 nm, respectively. In addition, the fraction of pores larger than 50 nm in the latter two samples is obviously higher than in ATO-400. The higher surface area of ATO-400 than the other two samples can be understood that the amorphous carbon possesses a lower density and higher porosity than the crystalline ATO. As the temperature increases, the micropores collapse which give rises to larger pores. The inter-particle connection also becomes looser when the crystallites grow larger.

The electrochemical performances of the ATO nanofibers as anodes in LIB were first investigated using CV and the curves for ATO-400 are shown in Figures 7a. In the first cathode scan, a broad reduction peak of about 1.2 V and 0.5 V was observed, which disappeared in the following cycles. These peaks correspond to the formation of the solid electrolyte interphase (SEI) layer on the electrode surface and reduction of ATO by lithium to form metallic Sn, Sb and amorphous Li_2O [19]. In addition, a strong reduction peak was observed at 0.75 V, The reason for this is that Li3Sb is formed by the reaction of Sb with Li+ .The multi-step alloying reaction between Sn and Li, which leads to the formation of LixSn, is shown by a broad peak around 0.4V. There is no significant difference between the three samples in terms of the redox profiles as the amorphous carbon in ATO-400 is not involved in the lithiation/delithiation process (Figure S4 shows CVs of ATO-500 and ATO-600). During the anodic scan, the oxidation peaks in the range 0.6-0.8 V in the first anodic cycle are due to dealloying reaction of LixSn, The oxidative peak at 1.1 V is due to the Li-Sb dealloying reaction [20, 21]. The interactions between Li^+, ATO, Sn and Sb can be described by the following reactions:

$$(Sn^{4+}Sb^{3+})O_{3.5} + 7Li^+ + 7e^- \rightarrow Sn + Sb + 3.5Li_2O \quad (1)$$

$$Sb + 3Li^+ + 3e^- \leftrightarrow Li_3Sb \quad (2)$$

$$Sn + 4.4Li^+ + 4.4e^- \leftrightarrow Li_{4.4}Sn \quad (3).$$

The independent lithiation processes of Sn and Sb endows ATO with excellent stability, as the inactive element can act as a buffer during lithiation of the other one.

The charge-discharge curves in the first cycle for the ATO nanofibers tested at a current density of 0.2 A g^{-1} are shown in Figure 7b. All the curves exhibited similar profile, and the three samples exhibited similar initial discharge capacities, i.e. The initial discharge capacities were 1563 mA h g^{-1}, 1662 mA h g^{-1} and 1711 mA h g^{-1} and the initial Coulombic efficiencies were 61.8%, 62.9% and 61.5% for ATO-400, ATO-500 and ATO-600, respectively. Both the discharge capacity and Coulombic efficiency for the first cycle are close to the good values reported for Sn-based electrodes, suggesting that the initial capacity is primarily determined by the grain size and crystallinity of Sn (and SnO_2) [22]. The large initial capacity loss is mainly related to the decomposition of the electrolyte, formation of an SEI layer on the carbon surface and the irreversible process of Li_2O formation, which is a characteristic of metal oxide anode materials [17, 21, 23].

The rate performances of the ATO nanofibers were assessed in the current range between 0.1 A g^{-1} and 3.2 A g^{-1}, with 10 cycles performed at each current and the results are shown in Figure 7c. It can be seen at a current density of 3.2 A g^{-1}, ATO-400 still delivers a capacity of 327 $mAhg^{-1}$ which is significantly higher than that of ATO-600 (81 $mAhg^{-1}$). Furthermore, the discharge capacity of the three samples recovered to 794 $mAhg^{-1}$, 774 $mAhg^{-1}$ and 610 $mAhg^{-1}$ as the current density returned to 0.2 Ag^{-1}, respectively. The excellent rate performance of ATO-400 is thought to be due to that larger surface area provides more reaction sites and shorter diffusion path of Li^+ during insertion and extraction. It is noted the rate performance of ATO-500 is comparable to that of ATO-400 despite it possesses a lower surface area. This might be related to its optimal pore size which could facilitate the ion transportation and thus compensates the effect of lower surface area.

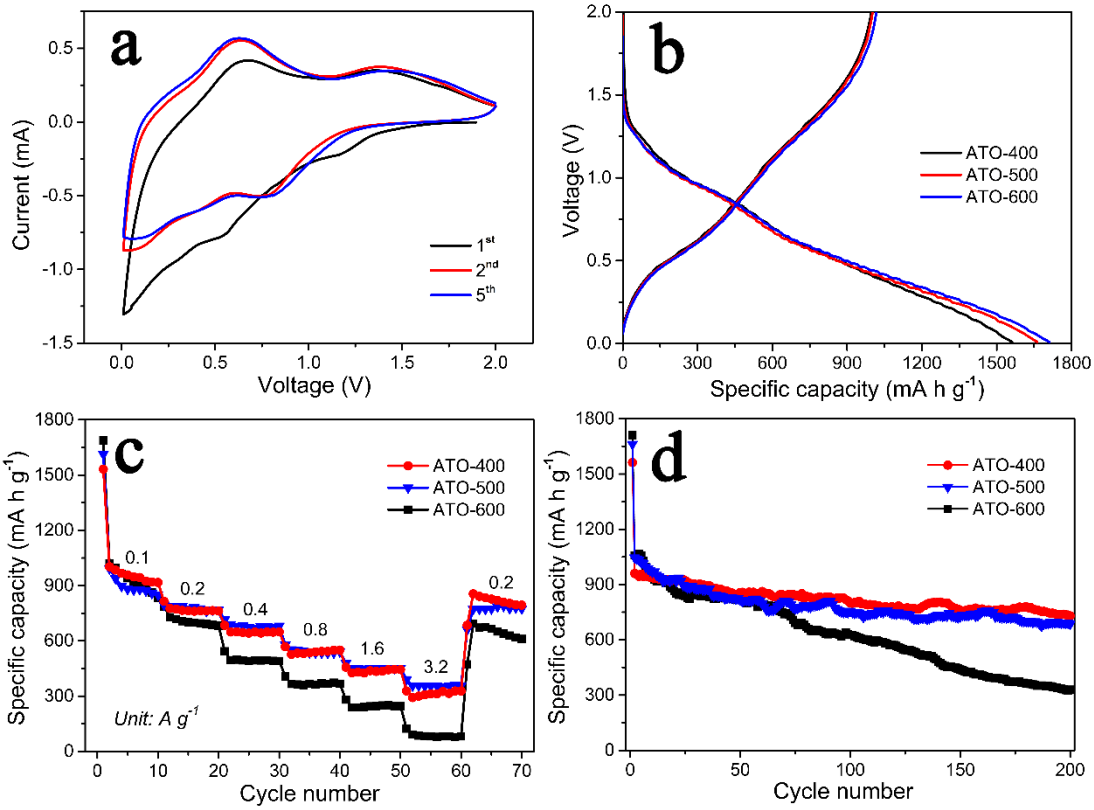

Figure 7. Electrochemical of ATO nanofibers: (a) CV curves, (b) the initial charge-discharge curves at 0.2 Ag^{-1}, (c) the capacities at different currents and (d) cyclic performance

The cyclic performance was examined at a current density of 0.2 Ag^{-1} for 200 cycles. It can be seen from Figure 7d that the decay of capacity for ATO-400 is less serious than those prepared at higher temperatures. At the 200th cycle, the discharge capacities of ATO-400, ATO-500 and ATO-600 samples were 730 $mAhg^{-1}$, 685 mA h g^{-1}, 329 $mAhg^{-1}$, and the corresponding capacity retentions relative to the second cycle were 76%, 66% and 32%, respectively. The capacity retention at the 200th cycle for ATO-400 is significantly higher than those reported for ATO nanostrucutres [24] (54% at the 30^{th} cycle) and composite of carbon nanotubes and Sn/SnO_2 ultrafine nanoparticles [9]. The better cyclic performance of ATO-400 than those prepared at higher temperature could be due to that the residual carbon can effectively alleviate the volume changes during cycling [1, 2, 25].

In Figure 8, the electrochemical impedance spectroscopy (EIS) of the ATO nanofiber composite was measured in the first cycle and the 100th cycle. The impedance spectrum exhibits a concave semicircle at high frequencies and a sloped line at lower frequencies, fitted by an equivalent. The circuit is shown in the inset of Figure 8a. In the equivalent circuit, Re is the resistance of the electrolyte, Rct is the resistance and charge transfer of the surface film, and Ws is the Warburg impedance CPE associated with the Li+ volume diffusion resistance. Component, [9, 26]. The fitted values of Re and Rct are summarized in Table 1. For the three ATO nanofibers, Rct increased significantly after 100 charge and discharge cycles, which is attributable to large volume changes during SEI film formation and cycling [27, 28]. Comparison of the three samples showed that the increase in Rct became more pronounced as the calcination temperature increased, confirming that

stable SEI film formation and residual carbon are critical to the cycling stability of the ATO-based electrode.

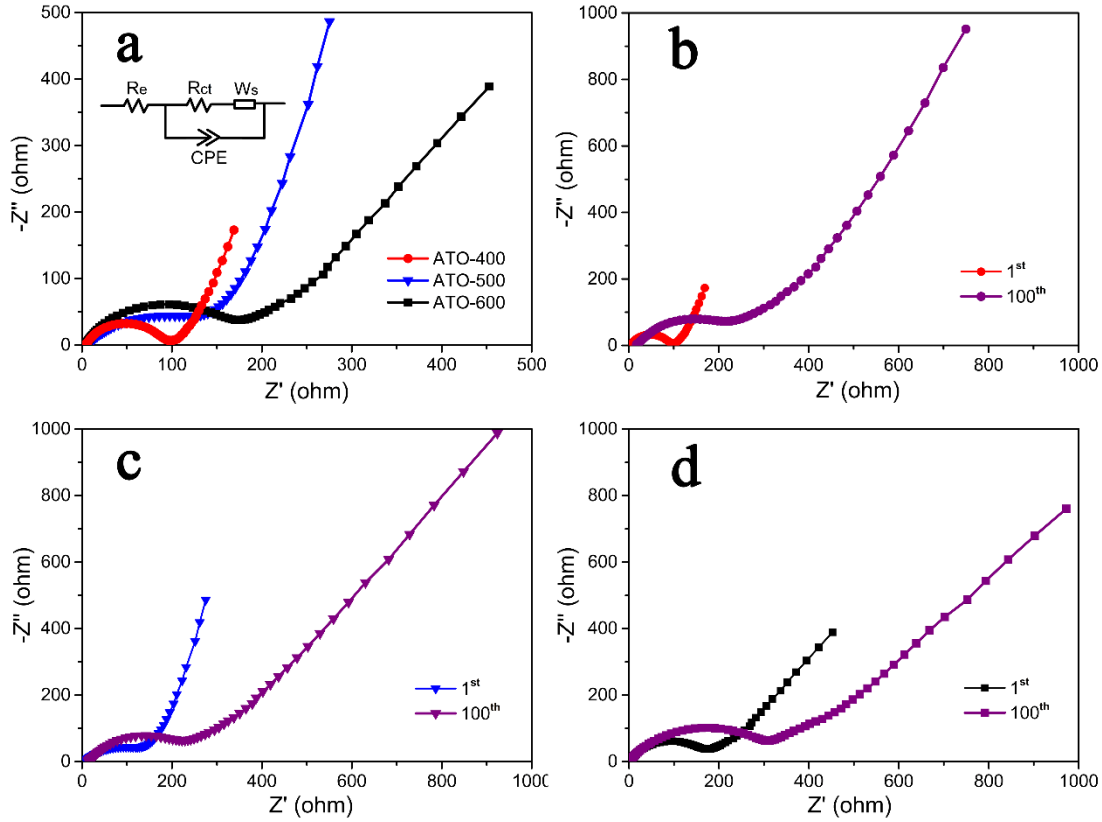

Figure 8. EIS spectra of ATO nanofibers: (a) before cycling, and ad different cycles for: (b) ATO-400, (c) ATO-500 and (d) ATO-600. Inset to (a) is the equivalent circuit.

Table 1. EIS fitting results for ATO nanofibers electrode.

	ATO-400		ATO-500		ATO-600	
	1st	100th	1st	100th	1st	100th
R_e (Ω)	3.9	14.5	6.2	11.8	4.1	11.9
R_{ct} (Ω)	86.5	186.7	77.4	225.5	165.7	309.1

To further investigate the stability of the electrodes during charge/discharge, the batteries were disassembled and the morphology of the electrodes was examined again using SEM. Figure 9 shows the images of ATO-400 and ATO-600 electrodes after 200 cycles of charge/discharge. It can be seen the fibrous morphology is retained and the particles are still embedded (or attached) intimately in the carbon matrix after 200 cycles for ATO-400, and no appreciable change in particle size upon charge/discharge is observed (Figures 9a and 9b). In contrast, the average particle size decreased remarkably in ATO-600 and part of the hollow fibers started to break down, suggesting severe pulverization of this anode (Figures 9c and 9d). The pulverization of ATO-600 was also confirmed by the easy separation of the electrode material from the copper foil. These results confirmed that ATO-400 possesses higher stability than ATO-600.

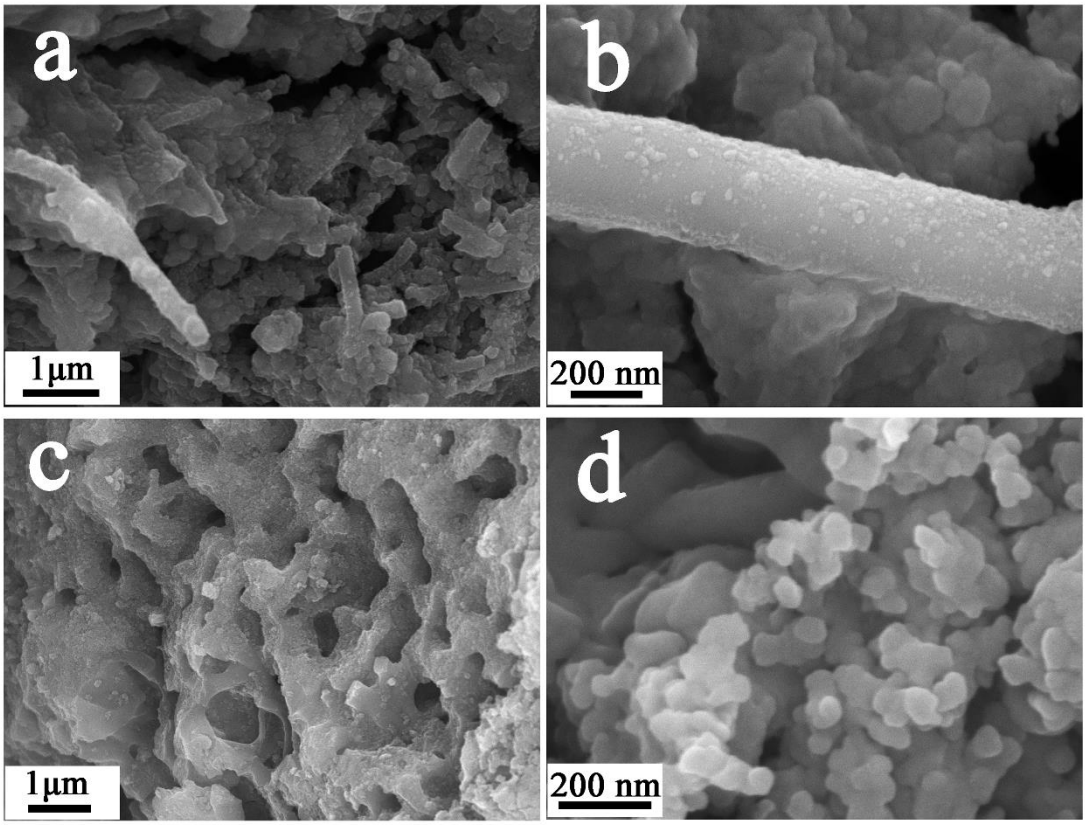

Figure 9. SEM images at different magnifications for the electrodes after 200 cycles of charge and discharge: (a) and (b) ATO-400; and (c) and (d) ATO-600.

4. CONCLUSIONS

In summary, it has been demonstrated that the morphology of $SnCl_2$/$SbCl_3$/PVP-derived ATO nanofibers develops from solid to hollow structures as the calcination temperature increases from 400°C to 600°C, which was explained by bi-directional concentration gradients and different diffusion rates of the metal chlorides and oxides. As shown in Table 2, we compare the materials of this work with other tin / antimony materials already reportedWhen tested as anodes in LIBs, all the ATO nanofibers exhibit a high initial capacity.

In addition, the cyclic stability and rate performance of the fibers calcinated at 400°C are superior to those treated at 600°C, and are also better than the good results reported for SnO_2-based anodes. The excellent electrochemical performance was attributed to the nano-fibrous structure and the carbon matrix which can accommodate the volume expansion and provide short diffusion lengths for lithium ions and maintain the integrity during cycling. The results shown in this study reveal the importance of the combination of carbon composition and fibrous structure for the SnO_2-based anodes, which would pave the way for further improvement of performance of LIBs.

Table 2. The electrochemical properties of the prepared SnCl2/SbCl3/PVP and other lithium battery negative electrode nanofibers were reported in the literature.

Structure	Current density (mA·g−1)	Cycle	Capacity reservation (mAh·g−1)	Mass loaded	reference.
Sn-SnSb/C c	779	1200	378	97%	[29]
SnSb@rGO@ CMF	350	200	318.5	68.2%	[30]
Tin/PCNFS	800	200	774	39.4%	[31]
SneSnSb	705	200	500	--	[32]
Sb/MoS2/C	763	150	679.5	--	[33]
SnCl2/SbCl3/PVP	1563	200	730	76%	This work

SUPPORTING INFORMATION

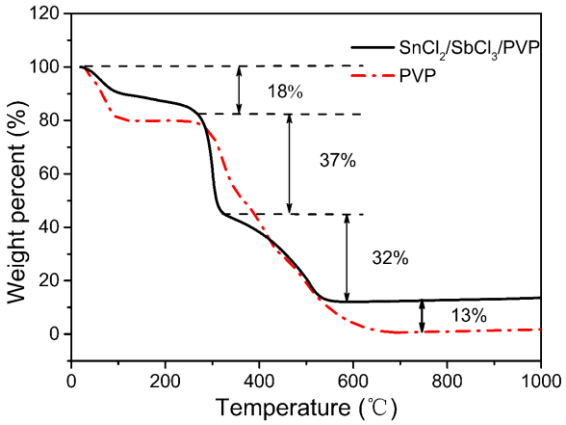

Figure S1 TG analysis of the ATO nanofibers and PVP fibers

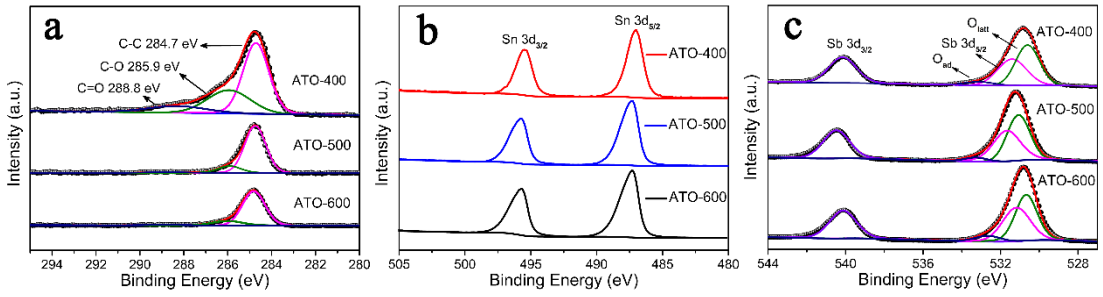

Figure S2 Deconvolved XPS spectra of the ATO nanofibers: (a) C_{1s} spectra, (b) Sn_{3d} spectra, and (c) Sb_{3d} and O_{1s} spectra.

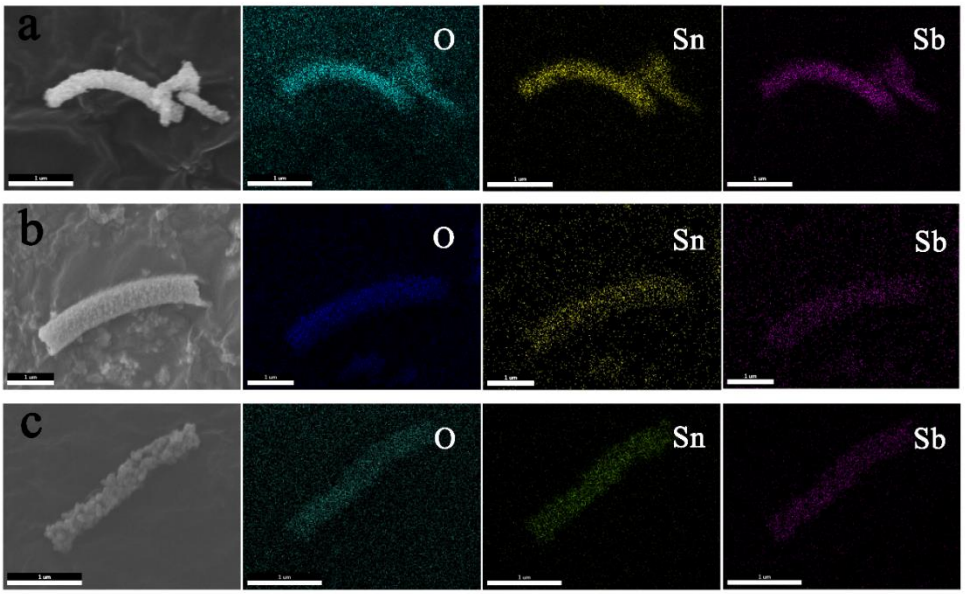

Figure S3 Elemental mapping images of the ATO nanofibers: (a) ATO-400, (b) ATO-500 and (c) ATO-600.

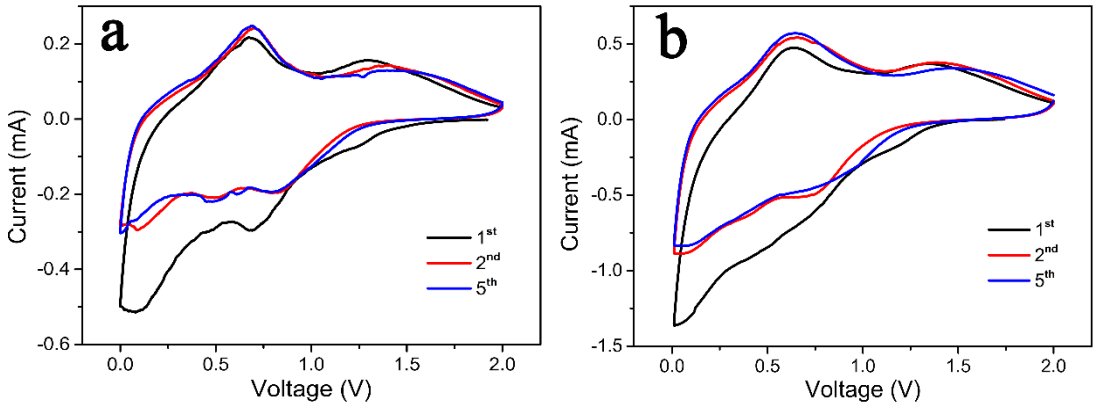

Figure S4 Cyclic voltammogram curves of ATO nanofibers: (a) ATO-500 and (b) ATO-600.

ACKNOWLEDGEMENTS

This work was financially supported by the National Natural Science Foundation of China (No. 51374146, 51502177), the Natural Science Foundation of Guangdong (No. 2016A030313057, 2015A030313542, 2014A030310323 and 2015A030310087), the Shenzhen Dedicated Funding of Strategic Emerging Industry Development Program (No. JCYJ20140418182819155 and JCYJ20150324141711596).

References

1. C.S. Niu, J.S. Meng, X.P. Wang, C.H. Han, M.Y. Yan, K.N. Zhao, X.M. Xu, W.H. Ren, Y.L. Zhao, L. Xu, Q.J. Zhang, D.Y. Zhao, L.Q. Mai, *Nat. Commun.*, 6 (2015).

2. H.-G. Wang, S. Yuan, D.-L. Ma, X.-B. Zhang, J.-M. Yan, *Energy. Environ.Sci.*, 8 (2015) 1660-1681.
3. L. Liu, F. Xie, J. Lyu, T. Zhao, T. Li, B.G. Choi, *J.Power Sources*, 321 (2016) 11-35.
4. J.S. Chen, X.W. Lou, *Small*, 9 (2013) 1877-1893.
5. K. Shiva, H.B. Rajendra, A.J. Bhattacharyya, *ChemPlusChem*, 80 (2015) 516-521.
6. K. Chen, X. Wang, G. Wang, B. Wang, X. Liu, J. Bai, H. Wang, *Chem. Eng. J.,* 347 (2018) 552-562.
7. A. Eftekhari, *Energy Storage Materials,* 7 (2017) 157-180.
8. A. Birrozzi, R. Raccichini, F. Nobili, M. Marinaro, R. Tossici, R. Marassi, *Electrochim.Acta*, 137 (2014) 228-234.
9. Y. Hu, Q.-R. Yang, J. Ma, S.-L. Chou, M. Zhu, Y. Li, *Electrochim.Acta*, 186 (2015) 271-276.
10. H. Peng, R. Li, J. Hu, W. Deng, F. Pan, *ACS appl. mate. inter.*, 8 (2016) 12221-12227.
11. B. Huang, Z. Pan, X. Su, L. An, *J. Power Sources*, 395 (2018) 41-59.
12. A.R. Babar, S.S. Shinde, A.V. Moholkar, C.H. Bhosale, J.H. Kim, K.Y. Rajpure, *J. Alloys Compd.*, 505 (2010) 416-422.
13. S.S. Kim, H.G. Na, Y.J. Kwon, H.Y. Cho, H.W. Kim, *Met. Mater. Int.*, 21 (2015) 415-421.
14. J. Luo, X. Luo, J. Crittenden, J. Qu, Y. Bai, Y. Peng, J. Li, *Environ.Sci.Technol.*, 49 (2015) 11115-11124.
15. P. Liu, Y. Zhu, J. Ma, S. Yang, J. Gong, J. Xu, *Colloids Surfaces A*, 436 (2013) 489-494.
16. H. Xiang, Y. Long, X. Yu, X. Zhang, N. Zhao, J. Xu, *CrystEngComm.*, 13 (2011) 4856.
17. X. Xia, *Express Polymer Letters*, 6 (2011) 169-176.
18. X. Xia, Y. Wang, A. Ruditskiy, Y. Xia, *Adv.. materials.,* 25 (2013) 6313-6333.
19. J.M. Kim*, Nano*, 10 (2015) 131-138.
20. M.V. Reddy, G.V.S. Rao, B.V.R. Chowdari, *J.Solid State Electr.*, 17 (2013) 1765-1773.
21. M.V. Reddy, G.V.S. Rao, B.V.R. Chowdari, *J. Mater. Chem.*, 21 (2011) 10003-10011.
22. Z. Shen, Y. Hu, Y. Chen, R. Chen, X. He, X. Zhang, H. Shao, Y. Zhang, *Electrochim. Acta*, 188 (2016) 661-670.
23. J.S. Cho, Y.C. Kang, *Small*, 11 (2015) 4673-4681.
24. W. Feng Dan, W. Minghong, W. Yong, *Electrochem. Commun.*, 13 (2011) 433-436.
25. D. Ma, Y. Li, P. Zhang, A.J. Cooper, A.M. Abdelkader, X. Ren, L. Deng, *J.Power Sources*, 311 (2016) 35-41.
26. S.Y. Kim, B.-H. Kim, *Synthetic Metals,* 210 (2015) 386-391.
27. Z.P. Guo, Z.W. Zhao, H.K. Liu, S.X. Dou, *Carbon*, 43 (2005) 1392-1399.
28. P. Zhang, Y. Wang, J. Wang, D. Zhang, X. Ren, Q. Yuan, *Electrochim. Acta*, 137 (2014) 121-130.
29. Z. Li, J. Zhang, J. Shu, J. Chen, C. Gong, J. Guo, L. Yu, J. Zhang, *J.Power Sources*, 381 (2018) 1-7.
30. H. Jia, M. Dirican, J. Zhu, C. Chen, C. Yan, P. Zhu, Y. Li, J. Guo, Y. Caydamli, X. Zhang, *J. Alloys Compd*, 752 (2018) 296-302.
31. J. Wang, W.-L. Song, Z. Wang, L.-Z. Fan, Y. Zhang, *Electrochim. Acta*, 153 (2015) 468-475.
32. S. Jena, A. Mitra, A. Patra, S. Sengupta, K. Das, S.B. Majumder, S. Das, *J.Power Sources*, 401 (2018) 165-174.
33. Y. Huang, C. Ji, Q. Pan, X. Zhang, J. Zhang, H. Wang, T. Liao, Q. Li, *J.Alloys Compd.*, 728 (2017) 1139-1145.

© 2018 The Authors. Published by ESG (www.electrochemsci.org). This article is an open access article distributed under the terms and conditions of the Creative Commons Attribution license (http://creativecommons.org/licenses/by/4.0/).